




Interaction of solar jets with filaments: Triggering of large-amplitude filament oscillations[★]

Reetika Joshi^{1,2} , Manuel Luna^{3,4} , Brigitte Schmieder^{5,6,7}, Fernando Moreno-Insertis^{8,9}, and Ramesh Chandra¹⁰ 

¹ Institute of Theoretical Astrophysics, University of Oslo, PO Box 1029 Blindern, 0315 Oslo, Norway
e-mail: reetika.joshi@astro.uio.no

² Rosseland Centre for Solar Physics, University of Oslo, PO Box 1029 Blindern, 0315 Oslo, Norway

³ Departament Física, Universitat de les Illes Balears, 07122 Palma de Mallorca, Spain

⁴ Institute of Applied Computing & Community Code (IAC³), UIB, Spain

⁵ LESIA, Observatoire de Paris, Université PSL, CNRS, Sorbonne Université, Université de Paris, 5 place Janssen, 92290 Meudon Principal Cedex, France

⁶ Centre for mathematical Plasma Astrophysics, Dept. of Mathematics, KU Leuven, 3001 Leuven, Belgium

⁷ SUPA, School of Physics and Astronomy, University of Glasgow, Glasgow G12 8QQ, UK

⁸ Instituto de Astrofísica de Canarias, 38200 La Laguna, Tenerife, Spain

⁹ Departamento de Astrofísica, Universidad de La Laguna, 38206 La Laguna, Tenerife, Spain

¹⁰ Department of Physics, DSB Campus, Kumaun University, Nainital 263 001, India

Received 8 December 2022 / Accepted 30 January 2023

ABSTRACT

Context. Large-amplitude oscillations (LAOs) are often detected in filaments. Using multi-wavelength observations, their origin can be traced back to the interaction with eruptions and jets.

Aims. We present two different case studies as observational evidence in support of 2.5D numerical magnetohydrodynamics (MHD) experiments that show that the LAOs in the filament channels can be initiated by solar jets.

Methods. We use longitudinal magnetic field observations using the Helioseismic Magnetic Imager to study the evolution of the filament channels. The LAOs in the filaments are analysed using two techniques. The first is time-distance diagnostics with extreme-ultraviolet (EUV) and H α datasets. In the second method, the oscillations in different parts of the filaments are examined using Fourier analysis of the brightness variations of all pixels in H α observations.

Results. In the two studied events, we can identify a quadrupolar configuration with an X-point at the top of the parasitic region suggestive of a classical null-point. The X-point evolves into a flat structure suggestive of a breakout current sheet. A reconnection flow emanates from this structure, leading to a jet that propagates along the filament channel. In both cases, we can identify the quiescent and eruptive phases of the jet. The triggered LAOs have periods of around 70–80 min and are damped after a few oscillations. The minimum magnetic field intensity inferred with seismology for the filament turns out to be around 30 Gauss.

Conclusions. We conclude that the two case studies are consistent with a recently published numerical model in which the LAOs are initiated by jets. The relationship between the onset of the jet and filament oscillations is straightforward for the first case but is less clear for the second case. In the second event, although there is some evidence for a relationship, we cannot rule out other possibilities such as activity unrelated to the null-point or changes in the magnetic structure of the filament. Both jets are associated with very weak flares that did not launch any EUV waves. Therefore, a role of EUV waves in triggering the filament oscillations can be eliminated for these two cases.

Key words. Sun: activity – Sun: filaments, prominences – Sun: flares – Sun: magnetic fields – Sun: oscillations

1. Introduction

Solar filaments (or prominences) are clouds of dense and cool plasma hanging in coronal heights (Labrosse et al. 2010; Mackay et al. 2010; Gibson 2018) and their origin is magnetic in nature. Occasionally, the active as well as the quiet filaments can oscillate. According to their amplitude, the oscillations can be divided into two categories. If the amplitude velocity is larger than 10 km s^{-1} , they are termed large-amplitude oscillations (LAOs); otherwise they are known as small-amplitude oscillations. The oscillations are also grouped according to the relative direction of their motion with respect to the promi-

nence magnetic field. When the motion is mainly in the assumed direction of the field lines, the oscillations are called ‘longitudinal’; when perpendicular to them, the oscillation is called ‘transverse’. In this paper, we consider only the longitudinal case, studying two large-amplitude longitudinal oscillation (LALO) events.

For a long time now, oscillations in solar filaments have been observed. In early observations, they were called winking filaments, as they were seen to move in and out of relatively narrow bandpasses (Hyder 1966; Ramsey & Smith 1966; Vršnak 1993). However, the first clear detection of a LALO is recent, and was reported by Jing et al. (2003), where the authors described the cold plasma of the prominence oscillating along the filament spine. Further cases have since been reported (see e.g., Vršnak et al. 2007; Zhang et al. 2012; Luna & Karpen 2012;

[★] Movies associated to Figs. 3 and 13 are available at <https://www.aanda.org>

Luna et al. 2014, 2017). Observations show that LALOs have periods of a few tens of minutes up to 160 min, although they mostly have periods of close to 1 h (Luna et al. 2018). Recently, Luna et al. (2022b) showed theoretically that the period can never exceed 167 min. In these oscillations, the filament threads move along the dipped magnetic field lines. Luna & Karpen (2012) proposed a so-called pendulum model where the restoring force is mainly gravity projected along the field lines. The gas pressure gradient also contributes, although it is considerably smaller than the gravitational force (Zhang et al. 2012; Luna et al. 2012). In the pendulum model, the period is given exclusively by the average radius of curvature of the dipped field lines (see also Roberts 2019). More studies based on 2D and 3D numerical simulations confirmed that the pendulum model describes the longitudinal oscillations quite well (Luna et al. 2016; Zhou et al. 2018; Zhang et al. 2019; Adrover-González & Terradas 2020; Liakh et al. 2020, 2021).

The trigger for the LAOs is identified variously as Moreton or extreme-ultraviolet (EUV) waves (Eto et al. 2002; Okamoto et al. 2004; Asai et al. 2012; Liu et al. 2012; Devi et al. 2022), shock waves (Shen et al. 2014), filament eruptions (Isobe et al. 2007; Chen et al. 2008), flares (Vršnak et al. 2007; Li & Zhang 2012), or jets (Luna et al. 2014; Zhang et al. 2017; Tan et al. 2023). These active phenomena perturb the filaments, and produce significant displacements with respect to the equilibrium configuration. In general, the displacements are larger in LALOs than in the case of transverse oscillations (Schmieder et al. 2013; Ofman et al. 2015). Jing et al. (2003) and Luna et al. (2017) reported LALOs with velocity amplitudes on the order of 100 km s^{-1} .

Nowadays, it is unclear how the different energetic events can excite the different polarisations of the LAOs. Only a few works have considered this problem. Liakh et al. (2020) studied a flux-rope prominence and a very energetic external disturbance. They found that both longitudinal and transverse LAOs are excited. More recently, Luna & Moreno-Insertis (2021) carried out the first theoretical study of the interaction between a jet and a prominence, finding that jets produce LALOs but also transverse oscillations. These jets are thought to arise due to the rearrangement of the magnetic field structure in the atmosphere caused by either magnetic flux emergence from beneath the solar surface; a driving process of the footpoints of the field lines through photospheric flows; or the induced stress in the coronal magnetic field, with a huge release of magnetic energy as a jet or small flare (Joshi et al. 2021a,b; Joshi 2022). Whatever the precise magnetic configuration or evolutionary structure leading to the jet eruptions, magnetic reconnection is well accepted to be present at the core of this process, converting the stored magnetic energy to kinetic energy of the jets (Joshi et al. 2020a,b; Schmieder et al. 2022; Schmieder 2022). In their model, Luna & Moreno-Insertis (2021) explain that the jets are produced in the sheared magnetic arcade near the footpoint of the filament channel. After multiple reconnection processes, the jet flows towards this filament channel and sets the filament into oscillations, with an amplitude of larger than 10 km s^{-1} .

In this paper, we present two different observational case studies of such an interaction between jet and filament. In both, the jet initiates the oscillations in the filament channel as suggested by Luna & Moreno-Insertis (2021). The first event on February 5, 2015, concerns an active region (AR) with a huge filament in its periphery. The AR was the site of repeated flux emergence events and consequently small flares and jets. For this case, we focus our study on one particular jet that hits one end

of the filament and initiates long time-period oscillations in the filament structure. The plasma material was pushed along or in the flux rope containing the filament and LAOs were observed. The second event was observed on January 1, 2014, and is chosen from the catalogue presented in Luna et al. (2018). It started with a few small-scale brightenings near one footpoint of the filament before the main jet, which flew towards the filament channel and set it into oscillation. As part of our conclusions, we show the similarities between observations and the model of Luna & Moreno-Insertis (2021).

2. Description of the observations and the oscillation analysis

The aim of this study is to give as complete a picture as possible of the interaction of coronal jets with prominences using data from several ground-based and space observatories. In addition, we also describe the technique we use to study and parameterise the oscillations in the prominences after jet impact.

2.1. AIA, $H\alpha$, and HMI observations

For the study of these two cases, we use the EUV data of high spatial and temporal resolution from the Atmospheric Imaging Assembly (AIA, Lemen et al. 2012) instrument on board the Solar Dynamics Observatory (SDO, Pesnell et al. 2012) satellite. AIA observes the full Sun in seven different UV and EUV wavebands. The pixel size and cadence of this instrument are $0.6''$ and 12 s respectively. In order to increase the contrast of the images, we deconvolved the EUV data using the AIA point-spread function with the routine `aia_deconvolve_richardsonlucy.pro` available in `solarsoft` (Freeland & Handy 1998). All the AIA images are co-aligned after correcting for the solar rotation and are plotted in logarithmic intensity scale. To get the best contrast for the filament and jet evolution, the multi-scale Gaussian normalisation processing technique (MGN; Morgan & Druckmüller 2014) was applied to the AIA images.

For the full-disk observations of the Sun from ground-based telescopes, we use the $H\alpha$ line-center photospheric data from the National Solar Observatory/Global Oscillation Network Group (NSO/GONG). To cover the Sun for the entire time of the day, there are six network telescopes situated all over the globe¹. The pixel size and temporal resolution of the $H\alpha$ data are $1''$ and 1 min, respectively. The filaments and their motions are most easily observed and tracked in $H\alpha$. We use GONG's $H\alpha$ images to support the AIA EUV observations. $H\alpha$ images show the dark filaments seen in absorption, which are in sharp contrast to the bright chromosphere around them.

In this study, we use the longitudinal magnetic field to show the evolution of the filament channels observed with the Helioseismic Magnetic Imager (HMI, Schou et al. 2012) on board SDO. The HMI provides the photospheric magnetograms with pixel size of $0.5''$ and a cadence of 45 s. For both of the studied events, we trace the magnetic history of the associated AR for a few hours previous to the jet filament interaction until its start time. Using the HMI magnetic field contours over-plotted on the EUV images, we identify the magnetic reconnection location near the jet base.

¹ <http://gong2.nso.edu>

2.2. Oscillation analysis technique and prominence seismology

To study the two events described in this work, we used the time–distance diagram technique as in Luna et al. (2014, 2017). For the first event, we used the GONG H α and the 171 Å SDO/AIA data (Sect. 3.3), whereas for the second event, we used 171 Å exclusively (Sect. 4.3).

We selected the 171 Å passband among all the AIA instrument filters because this passband shows not only the absorption due to the presence of the cool plasma prominence but also the prominence emission thought to be part of the prominence–corona transition region (PCTR) at temperatures $>4 \times 10^5$ K (Parenti et al. 2012). The PCTR is highly filamented, and therefore the 171 Å band, with its combination of prominence absorption and emission, can highlight fine structure, allowing us to track the oscillations: when laying an artificial ‘slit’ that crosses the moving filament (as detailed in Sects. 3.3 and 4.3) and plotting the brightness along the artificial slit by means of a time–distance diagram, clear oscillatory patterns become apparent. Hereafter, we use the term slit instead of artificial slit. We note that when we use the term ‘slit’ we refer to the path we use to measure the intensity and not to the slit of a spectrograph. The oscillatory curves can then be fitted to a damped sinusoidal curve of the form

$$s(t) = s_0 + A e^{-t/\tau} \sin\left(\frac{2\pi}{P}t + \varphi_0\right), \quad (1)$$

where s , A , P , τ , and φ_0 are the coordinate along the slit, amplitude, oscillation period, damping time, and the initial phase, respectively.

The study of oscillations with time–distance diagrams is restricted to a small portion of the filament along which we have traced the oscillations. However, as we show below, the jet reaches a large part of the filament and makes it oscillate. Therefore, in order to understand how the different parts of the filament oscillate beyond what is captured by the slit, we carry out a Fourier analysis of the brightness variations of all pixels in the GONG H α images using the technique recently developed by Luna et al. (2022a).

With this method, we can identify the regions that oscillate and the period of the oscillations. However, this technique cannot be used to extract the rest of the oscillation parameters, such as amplitude, damping time, or direction of motion.

Luna & Karpen (2012) showed that the period of the longitudinal oscillations is determined by the curvature of the dips that hold the plasma of the prominence in the so-called pendulum model (see also Zhang et al. 2012). This is because the dominant restoring force in the oscillation is gravity projected along the field lines (Luna et al. 2012). Recently, Luna et al. (2022b) extended the pendulum model by considering that the gravity is not uniform but changes its direction with the position over the solar surface. This introduces important effects for periods larger than 60 min. In addition, these latter authors found that the periods of the longitudinal oscillations cannot be longer than $P_\odot = 167$ min.

Luna et al. (2022b) explained the relation between the period P and the curvature of the dips R , as

$$\frac{R}{R_\odot} = \frac{(P/P_\odot)^2}{1 - (P/P_\odot)^2}, \quad (2)$$

where R_\odot is the solar radius. The authors also determined a minimum value of the magnetic field of the dipped lines in order to

have magnetic support of the cool mass. Using Eq. (27) from Luna et al. (2022b), we obtain

$$B(\text{Gauss}) = (47 \pm 24) \frac{P/P_\odot}{\sqrt{1 - (P/P_\odot)^2}}. \quad (3)$$

The term in the parentheses is computed assuming a typical density range for prominences of $\rho = 2 \times 10^{-11} - 2 \times 10^{-10} \text{ kg m}^{-3}$ (Parenti 2014). We consider the prominence density to be the most important source of uncertainty in the estimated magnetic field, because the uncertainties associated with the fit are smaller than the above density range. In the present work, we use these equations to compute the radius of curvature and magnetic field.

3. Event 1: February 5, 2015

The jet–filament interaction on February 5, 2015, started with the ejection of a solar jet parallel to the long filament near the AR 12280. This jet was associated with a circular flare in the AR and it set the filament into oscillation (see the animation [online](#)).

3.1. Environment of the filament and jet

This event concerns the active region NOAA AR 12280, which appeared on the solar disk on February 2, 2015, and was located at S08 E17 ($-282''$, $-33''$) on February 5 (Fig. 1). A succession of C-class X-ray flares related to several magnetic flux emergence events was registered by GOES during its disk passage (see Fig. 2): on February 2 (C 1.7 class flare), on February 3 (C 2.7 and C 1.5 class flares), and on February 4 (C 2.7, C 1.5, C 3.0 flares), and a B7.8 class flare was registered starting at 20:44 UT and peaking at 20:52 UT on February 5². These flares were accompanied by recurrent jets. We concentrate our study on the last event on February 5 at 20:44 UT.

The magnetic configuration of the AR consists of a complex polarity pattern with a leading positive polarity (top panels of Fig. 1). Successive new episodes of magnetic flux emergence were observed inside a remnant bipolar AR, consequently increasing the complexity of AR 12280. We show two examples: on February 3 there is a clear emerging bipole (red circle in panel a), and on February 5 a second emerging flux event is indicated by a blue oval in panel b. A large intermediate filament was located to the southeast of the AR along an extended polarity inversion line (PIL). The bottom row of Fig. 1 shows the AR in 171 Å for February 3 and February 5, 2015, where the filament is seen as a dark structure (shown with the white arrow). The filament has one end located over the AR near the origin of the jet. The jet initially pushes a large part of the filament and we see periodic motions of the mass, which moves back and forth along the filament spine (see [movie](#)).

3.2. Generation and evolution of the jet

The jet was associated with a circular flare and a bidirectional flow towards the east and north directions. Figure 3 shows a zoomed-in view around the jet. The figure contains deconvolved AIA 171 Å images; we use a black and white representation to increase the contrast. In Fig 3a, a dome- or arcade-shaped structure overlying the emerging bipole can be clearly identified with an ‘X’-point configuration at its top, strongly suggestive

² <https://www.spaceweatherlive.com/en/archive/2015/02/05/xray.html>

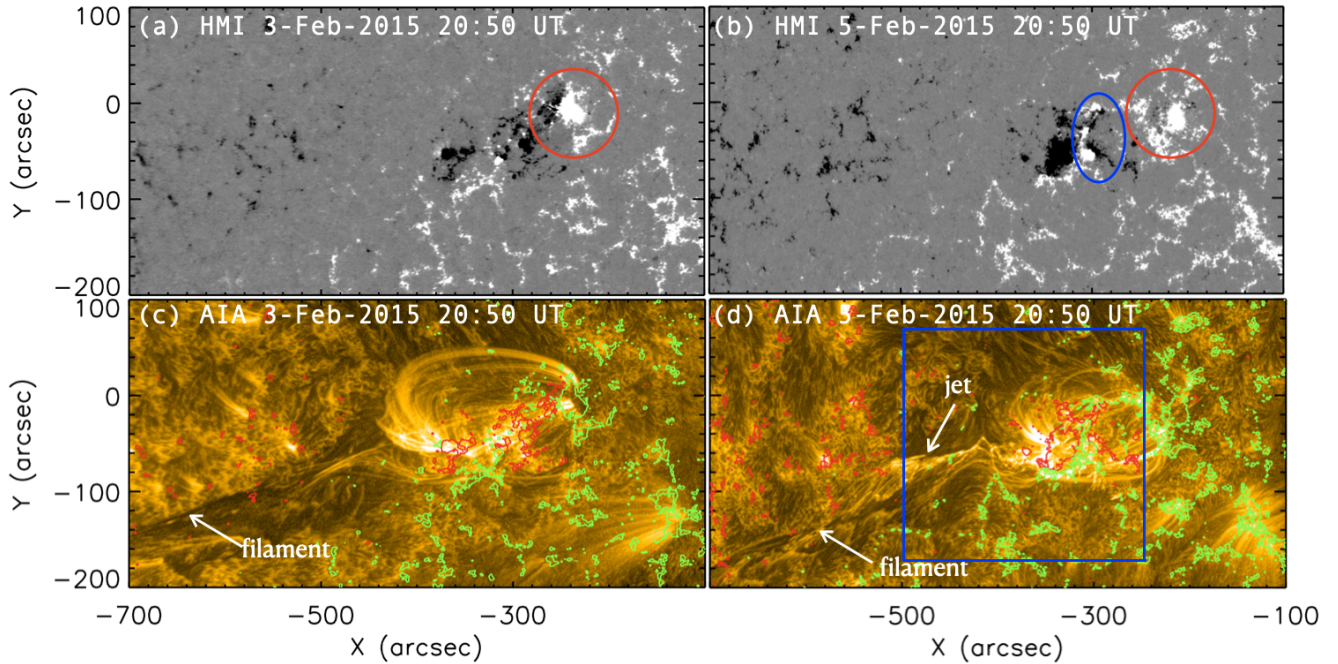


Fig. 1. Evolution of AR NOAA 12280 on February 3–5, 2015. Top panels: HMI magnetograms, bottom panels: AIA 171 images. The emergence of magnetic bipoles is clearly visible in the neighbourhood of the AR and near the jet base. Two examples: the red circle in the top panels a,b indicates a new emerging bipole on February 3; this was followed on February 5 by an another emerging bipole marked by the blue oval (panel b). The green and red contours are the HMI magnetic field contours of ± 100 Gauss in strength, respectively. The images are aligned together at 20:50 UT on February 5, 2015. The blue square is the FOV of Fig. 3.

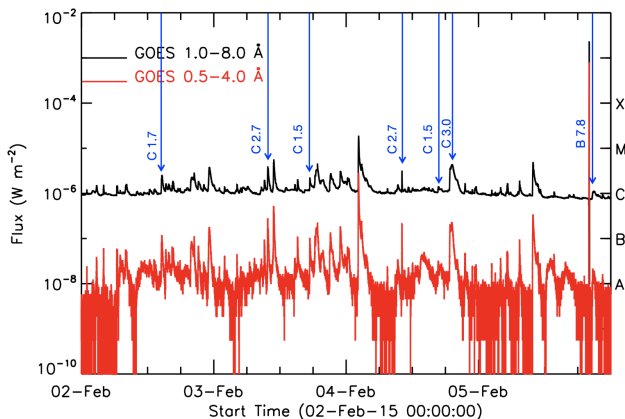


Fig. 2. Succession of flares in AR 12280 from February 2–5, 2015, registered by GOES. The jet eruption presented here is associated with the GOES B7.8 class flare on February 5 at 20:52 UT.

of a null-point structure (white arrow). A small filament (indicated by a red arrow in Fig. 3a) located under the magnetic arcade starts to erupt at 20:30 UT. During its eruption, it encounters the null-point-type configuration which leads to its collapse into a flat structure suggestive of a breakout current sheet (BCS; marked with yellow arrows in panels b–d). The configuration in panel b (20:50 UT) roughly corresponds to the time when the jet flows reach the filament; the succession of events leading to this configuration can be studied in more detail by comparing, as done in Fig. 4, the evolution in three different filters (AIA 171 Å, AIA 304 Å, and $H\alpha$ in the top, middle, and bottom rows, respectively) at times 20:40 UT, 20:44 UT, and 20:50 UT, in the left, centre, and right columns, respectively. The main reconnection flow issuing from the BCS leads to a

large jet that impinges onto the filament. This jet is apparent as a bright spine issuing from the BCS in the AIA 171 Å and AIA 304 Å filters at 20:44 UT and 20:50 UT, respectively (Fig. 4b, c, e and f). In the $H\alpha$ images (bottom row), the filament is seen to roughly coincide in position with the hot jet; also, the associated circular flare in the vicinity of the jet region is clearly visible in those three panels. Going back to Fig. 3, we can see some additional consequences of the jet ejection at times a little later than those shown in Fig. 4: in particular, we can see that, apart from the main reconnection flow leading to the large jet, there is a secondary flow issuing from the BCS and oriented in the north direction, as marked with cyan arrows in panels b–d of the figure.

The main jet moving towards the filament, sets it into oscillations. We use time–distance diagrams to study the propagation of the main jet and the filament oscillations (Fig. 5). The slit used for the diagrams is shown in panel a on the background of an AIA 171 Å image; the choice of this non-straight slit is such that its orientation follows the jet flow and direction of the plasma oscillations of the prominence. To match the general direction of the flow, distances along the slit are measured starting at the end nearest to the AR. Leaving the analysis of the oscillations to Sect. 3.3, we focus here (Fig. 5b) on the flows apparent in the time–distance diagram in the region of the slit nearest to the BCS, or, more precisely, in the 150'' starting to the top right of the slit. In the figure, we can see a complex structure with lots of bright paths. The slope of the bright paths is proportional to the flow velocity. The dashed lines indicate the trajectory of two such paths, one toward the beginning and the other toward the end of the jet ejection; the first one starts at 20:48 UT and has a projected speed of about 220 km s^{-1} while the second starts at 21:08 UT and has a projected speed of about 90 km s^{-1} . From those values, and from direct inspection of the inclination of the tracks in the figure, we conclude that the jet, which always

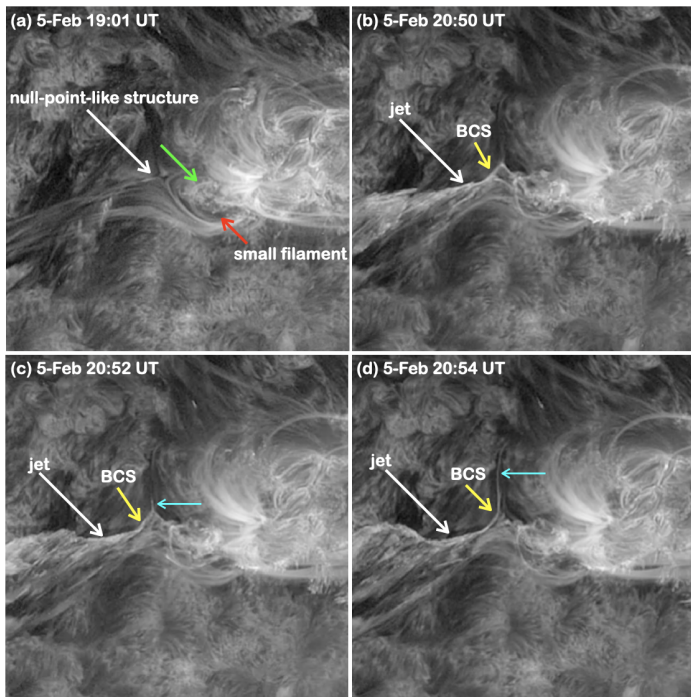


Fig. 3. Zoom image of the jet base in AIA 171 Å. The FOV for this figure is presented as the blue square in Fig. 1d. The null-point-like structure at the jet base is indicated with a white arrow (panel a). The jet is initiated under the arcade (green arrow) following a small filament eruption (red arrow). This small filament pushes the arcade towards the null-point-like structure, which leads to the jet flowing towards the filament (white arrow in panel b–d) in the southwest. This flow is bidirectional, as we observe the second branch, which flows toward the north, is indicated with cyan arrows in panels c–d. The null-point-type structure collapses into the breakout current sheet (BCS). The latter is marked using yellow arrows in panels b–d; see also the animation [online](#).

follows the same trajectory, decreases its velocity (and most probably also its kinetic energy flux) as time advances.

3.3. Filament oscillations

To study the oscillations caused by the impact of the jet, the time–distance diagram introduced above has to be extended to the full length of the slit and to a much longer time interval than shown in Fig 5b. The diagram used is shown in panel 5c, with the white box marking the limited domain used in panel 5b.

The jet flows reach the filament at 20:50 UT as we see in Sect. 3.2. The interaction produces a displacement of the prominence plasma along the slit. During the first 50 min, we see bright and dark features moving along the slit. We might describe this as the triggering phase where the jet flow interacts with the filament plasma. This plasma moves until it reaches maximum elongation at approximately 21:20 UT. Between this time and 02:00 UT, a clear oscillatory pattern can be identified in panel c. However, the movement of the prominence plasma is very complex with several especially prominent oscillation paths visible: the plasma probably oscillates at various levels with different periods and directions. Because of the difficulty in tracking the movement of a single path, we also use the $H\alpha$ data. Figure 5d shows the $H\alpha$ diagram constructed with the same slit. We can see that $H\alpha$ shows a bulk motion of the plasma that is consistent with an oscillation. We define a curve in the centre

of the dark band and then fit the oscillation using Eq. (1). The resulting fit is plotted in both panels c and d. The fit is very good in the $H\alpha$ diagram. In contrast, in AIA 171 Å, the curve does not appear to match any of the paths in the diagram. The adjusted period is 77 ± 2 min; however, in AIA 171 Å it seems that the period of the different threads ranges up to 120 min.

The variation with height of the oscillation period is known from a theoretical point of view (Luna et al. 2016). A similar behaviour was found by Raes et al. (2017), who pointed out that this effect could produce the false impression of vertically propagating waves. These authors called these apparent waves ‘super-slow modes’.

Beyond 02:00 UT on February 6, the oscillation disappears, as the filament configuration changes and the oscillation moves out of the slit. The rest of the oscillation parameters from the fit are the velocity amplitude of $33 \pm 5 \text{ km s}^{-1}$ and the damping time of $\tau = 196 \pm 74$ min. The ratio between the damping time and the oscillation period is $\tau/P = 2.5$, which indicates that the oscillation damping is relatively strong. Luna et al. (2018) found typical ratios $\tau/P = 1.25$ for LAOs, indicating strong damping of this kind of motion. Using Eq. (2), for a period of 77 min, we obtain a radius of the dips $R = 188$ Mm. In addition, with Eq. (3) we can also obtain a lower limit for the magnetic field intensity in the range $B = 12\text{--}37$ Gauss.

As we show above, the oscillations in the filament are quite complex, with several periodicities involved. Moreover, the analysis of the oscillations using a single slit is limited to a small area of the filament. To carry out a more complete study of the periodicities and to identify the regions of the filament that oscillate after the impact of the jet, we applied a technique developed by Luna et al. (2022a), as already mentioned in Sect. 2.2. This technique involves studying the periodic fluctuations of every pixel of the $H\alpha$ images from the GONG network. With the fast-Fourier transform, the power spectral density (PSD) is computed. To discriminate spurious fluctuations from the real oscillations, it is required that the peak in the PSD be greater than several times the background noise so that the confidence level is above 95%.

As shown in Fig. 6, the jet produces oscillations in a large part of the filament. The periods range from 60 to 110 min, which is in agreement with the 77 min obtained with the time–distance method. It is interesting to note that, at the northern end, a large area oscillates with periods of around 110 min. The spatial distribution of periods may be associated with the fact that we observe the oscillations along different field lines and these have different curvatures in their dips. Using Eq. (2), from the period range from 77–120 min, we obtain that the radius of the dip is in the range 103–534 Mm. Similarly, using Eq. (3) we obtain that the field strength in the filament ranges between 9 and 64 Gauss.

3.4. Comparison with the theoretical model of Luna & Moreno-Insertis (2021)

The observations presented in Sect. 3 bear remarkable similarities to what was described in the theoretical model of Luna & Moreno-Insertis (2021). In their model, the magnetic arcade associated with a bipolar parasitic region at the flanks of the filament channel (FC) of a prominence was sheared at its photospheric feet. The null point at the top of the parasitic region initially has a classical X-point shape; however, through the photospheric shear, the X-point evolves into a breakout current sheet (BCS) where reconnection takes place. The change in the magnetic configuration and associated reconnection lead to a succession of non-linear waves or jets (Alfvénic front, sonic front,

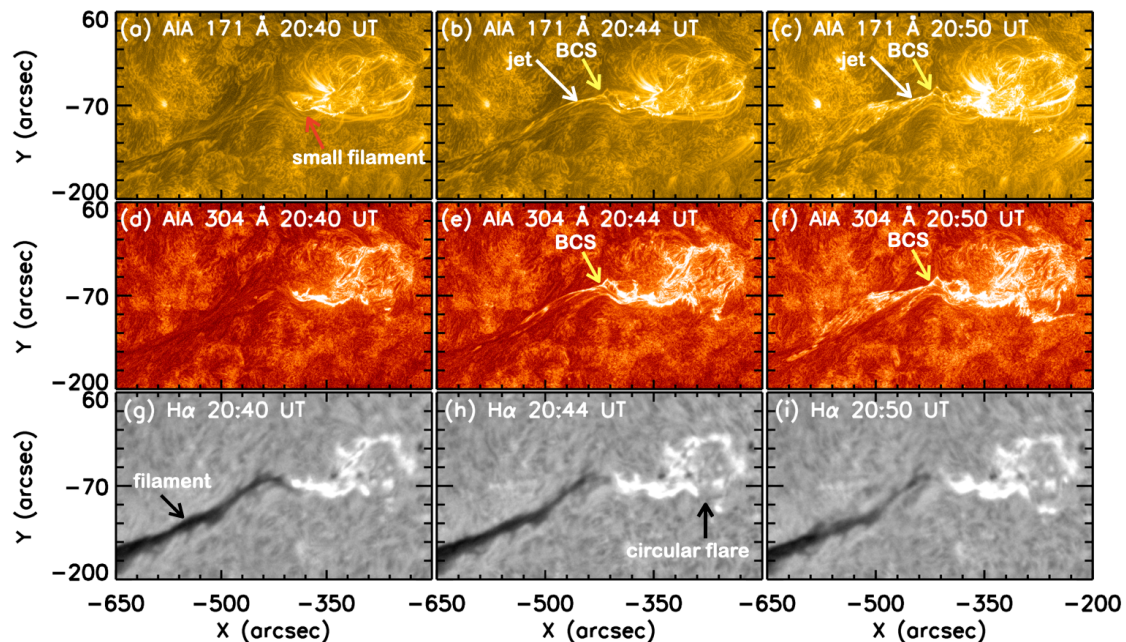


Fig. 4. Filament and jet evolution for event 1 on February 5, 2015, observed in AIA 171 Å (top row), AIA 304 Å (middle row), and H α (bottom row). The jet ejects from a dome-like structure with a small filament eruption shown in panel a. The jet flows towards the long filament through the breakout current sheet (BCS) shown in panels b, c, e, and f and a zoomed-in view is presented in Fig. 3. The long filament is well observed in all these channels as a cool and dense structure (shown in panel g). This jet is associated with a GOES B7.8 circular flare shown in panel h).

eruptive jet) that propagate along the filament channel eventually impacting the prominence. Most of the basic features of that model seem to be discernable in the observations. Starting with the null-point and BCS, the time series of events in AIA 171 Å (Fig. 3 and associated movie) seem to show precisely this kind of configuration: in Fig. 3a the AIA 171 Å image clearly delineates an X-point that subsequently evolves (panels b and c) into a flat BCS. In Fig. 7, we compare the electric current distribution at a relevant time in the numerical model – with its characteristic flat top – to Fig. 3b. There is a clear morphological and evolutionary similarity between the AIA 171 Å brightness patterns and the results of the model.

The non-linear waves and jets arising in the model as a result of the reconnection were produced in two stages. In the first one, an Alfvénic front followed by a more standard sonic shock were launched from the BCS; these are difficult to discern in the current observations. Then, in the second stage, reconnection in a quasi-vertical current sheet starts below the BCS; a twisted flux rope resembling a mini-filament is produced and hurled upwards against the BCS. There follows a violent eruptive jet that is launched along the field lines of the filament channel and eventually impacts the prominence. In the observations, we already mentioned the appearance of a small filament-like structure that erupts below the magnetic arcade (marked with a red arrow in Fig. 3) toward the BCS. More importantly, the major eruptive jet at ~20:50 UT (described above and shown in Figs. 3b–d and also in the animation (Fig. 4) clearly originates in one of the sides of the BCS and travels along the filament channel towards the filament. This matches the magnetic field and velocity patterns obtained in the numerical model quite well, as apparent in for example Fig. 12 of Luna & Moreno-Insartis (2021), adapted here with extra markers for ease of comparison (see Fig. 8). The two panels show the eruptive phase of the jet. In panel a, the yellow rectangle delimits the area where the near-vertical current sheet occurs during the eruptive phase of

the magnetic reconnection. The plasmoid originated in the vertical current sheet moves upwards and merges with the overlying field. The plasmoid moves at high velocity, as indicated by the almost vertical arrow in the figure. This produces a large perturbation, which generates flows that propagate along the field lines and collide with the prominence (see Fig. 8b). In contrast to the model, the jet in the observations shows a rotational motion along the filament channel with about one turn along the entire length between the BCS and the filament; this leads to a misalignment of about 30 deg between some of the branches of the jet and the filament spine. In the theoretical simulation, changes in field line orientation were seen propagating along the FC, but no real rotation of the plasma around the field lines of the FC could develop given the two-dimensional (more precisely 2.5D) nature of the model. Finally, in the numerical simulation, the side of the BCS opposite the filament also has an outflow, albeit much weaker than the main outflow and jets. This is apparent as a thin layer with velocity arrows pointing upwards and away from the BCS in Fig. 7. In the observation, as pointed out in Sect. 3, there is also a collimated brightening issuing from the BCS and pointing north (marked with cyan arrows in Fig. 3c,d). This is suggestive of the presence of a secondary outflow from the reconnection site also in the actual observed configuration.

4. Event 2: January 1, 2014

4.1. The host active region and the filament

On January 1, 2014, AR 11938 was located near disk centre (S09W03). This region consists (Fig. 9a,b) of disperse polarities (P0-N0); new emerging magnetic flux (EMF; P1-N1) appeared on December 31, 2013. That emergence occurred in the middle of the positive polarity P0, causing it to split into two main fragments; we use the notation P0' for the fragment that is closest to N0. There are several PILs in the AR (Fig. 9b). PIL1 is

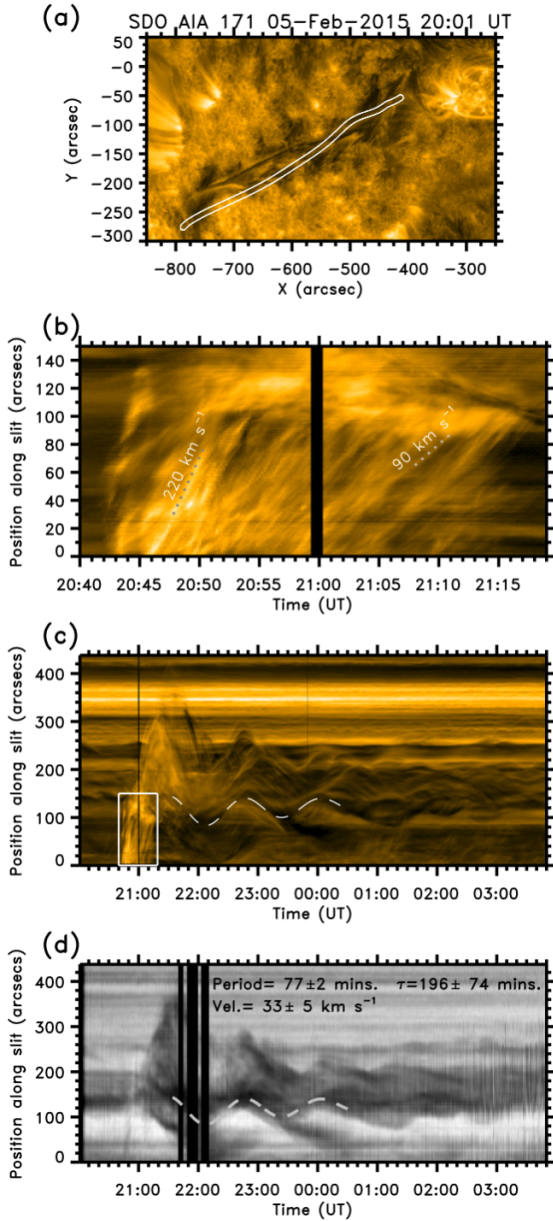


Fig. 5. Trace of the oscillations in the filament for the first event on February 5, 2015, observed with AIA 171 Å and H α . Panel a: filament seen in absorption in AIA 171 Å on February 5, 2015, with the artificial slit used to construct the time–distance diagrams (panels b–d) shown as a white contour. Panel b: time–distance diagram for the AIA171 image along the topmost 150'' of the slit; panel b in Fig. 3, taken at time 20:50 UT. Panels c and d contain the time–distance diagrams for the brightness along the curved slit, clearly showing the oscillatory patterns analysed in this paper. The white tracks in panels c and d show one of the fits obtained for the oscillation, which has a period of 77 min, velocity amplitude of 33 km s⁻¹, and a damping time of $\tau = 196$ min. The black vertical stripes in panels b, c, and d are data gaps.

between P0' and N0, and PIL3 is between P1 and N1 in the oval of panel b. We followed the evolution of the magnetic field for 12 hours before the eruption and observed the expansion of P1–N1 as the flux emergence process advances; between them there are mixed polarities, probably indicating sea serpent field lines, which originate from the edge of the sunspot and create moving magnetic features (MMFs; [Sainz Dalda & Bellot Rubio 2008](#)). During this expansion, a strong shear occurs between P0'

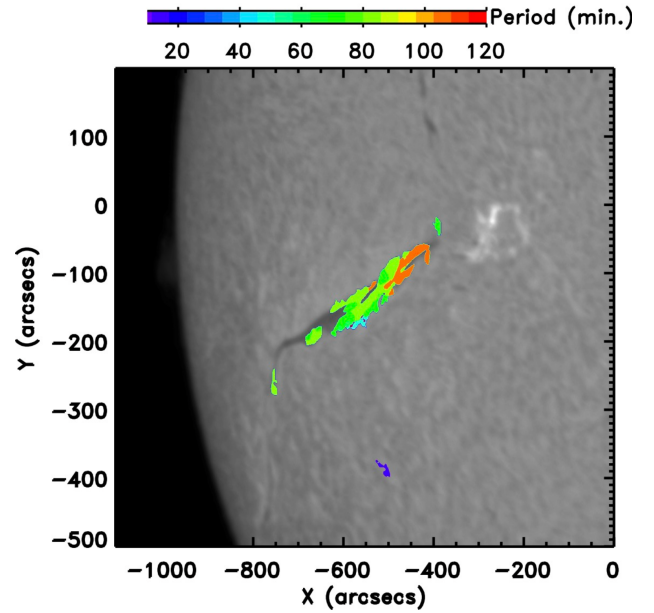


Fig. 6. Time periods of the filament oscillations over a GONG H α image on February 5, 2015, using the technique developed by [Luna et al. \(2022a\)](#). The colour code shows the periods in minutes.

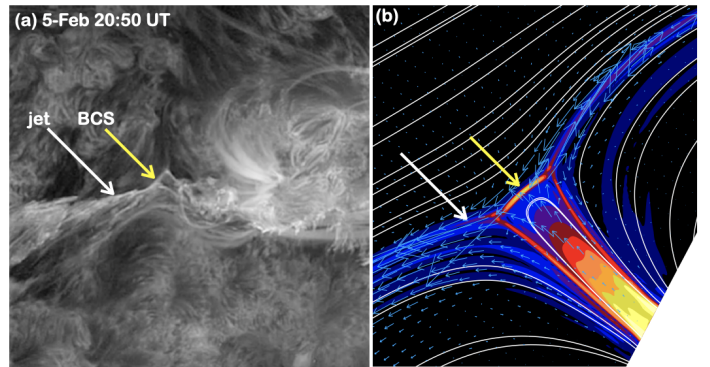


Fig. 7. Similarity between the observation of event 1 on February 5, 2015, and the numerical model of [Luna & Moreno-Inertis \(2021\)](#). The left panel is identical to panel b of Fig. 3; the right panel shows the electric current distribution of the model of [Luna & Moreno-Inertis \(2021\)](#) (adapted from their Fig. 4c). The flat breakout current sheet is marked in both panels by a yellow arrow.

and these mixed polarities. In panels c and d, the coronal emission counterpart can be seen in AIA 171 Å images, with green and red contours superimposed, marking the HMI polarities. In panel d, we can see a structure resembling a dome surmounted by a null-point or current sheet, probably associated with (and resulting from) the strong photospheric shear mentioned above (enclosed with the blue circle).

The best distinction between chromospheric, TR, and coronal structures, and the clearest view of the filament, can be gained by comparing simultaneous H α , AIA 304 Å, and AIA 171 Å images, as presented in Fig. 10. Looking at the H α panels (bottom row), the filament is clearly visible in the neighbourhood of NOAA AR 11938 and stretches mainly in the direction from southeast to northwest, with the southern tip touching the AR, which is also where the bright jet activity described below takes place; the top part of the filament is arched in the east–west direction. Both from Fig. 9c–d, and from the AIA 171 Å

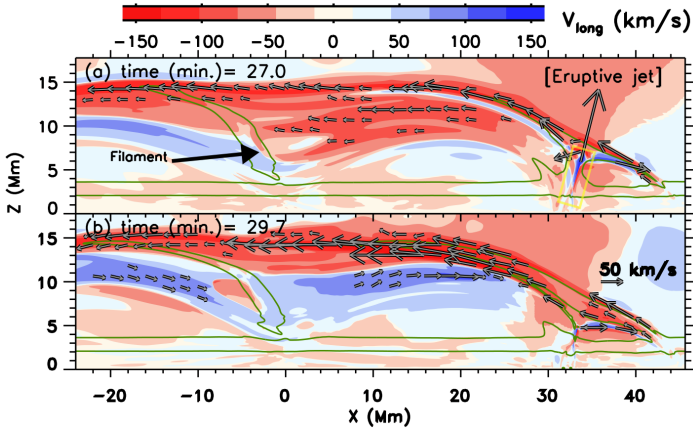


Fig. 8. Interaction of the ejected plasma with a filament channel adapted from Luna & Moreno-Insertis (2021). Both panels show the evolution of the jet at $t = 27$ (a) and $t = 29.7$ (b) minutes after the start of the numerical simulation. The green contours are isolines of the density. Around $x = 0$, we see the green contour of the filament suspended in dips of arcades of magnetic field (indicated by a black arrow in panel a). Red and blue are the velocity flows projected along the magnetic field lines. The vector field shows the flow velocity. For better visualisation, only vectors with a velocity greater than 20 km s^{-1} are shown. To show the scale of the velocity vectors, a 50 km s^{-1} arrow is shown on the right side of panel b.

and AIA 304 \AA snapshots of Fig. 10 (e.g., panels b and e), one sees that the filament has one end in the vicinity of the dome. The magnetic configuration near the dome appears to be quadrupolar again, as in the February event described in Sect. 3, and is therefore of the same type as that studied in the theoretical model of Luna & Moreno-Insertis (2021). The filament is sinistral according to the orientation of its lateral barbs in the $H\alpha$ images (Fig. 10g–i).

4.2. Jet activity

To follow the jet propagation from its source towards the filament channel, we analysed the AIA multi-wavelength observations in 171 and 304 \AA shown in Fig. 10 (top and middle rows) and, in full for 171 \AA , in an accompanying animation. Between 12:00 to 12:35 UT, we observe many small bright jets with short lifetimes. These emanate from the null-point-like structure going upwards in the direction of the filament. In Fig. 10a, we can see the hot plasma that has emanated from these jets as bright structures on the filament following the magnetic field lines of the filament channel. Right after 12:40 UT, a significant jet is observed: an intense brightening is seen around the area of the null point and the jet is accompanied by apparently larger flows than the previous cases (see the left black arrow in Figs. 10b and 10e), which can also be seen over the filament (right black arrow in Fig. 10b). Prior to 13:20 UT, no clear association of the jets with filament oscillations can be established. However, at 13:21 UT, an intense brightening (like a burst) is observed around the null-point. This brightening leads to a jet propagating on the left-hand branch issuing from the null-point-like structure more than in the direction of the filament (cyan arrow in Figs. 10c and 10f). Alternatively, this could be caused by activity unrelated to the null-point area. For example, at 13:22 UT at $x = -40$ and $y = 25$ arcsecs, a brightening occurs simultaneously with that of the null-point. However, we do not observe any flows impacting the filament from other regions.

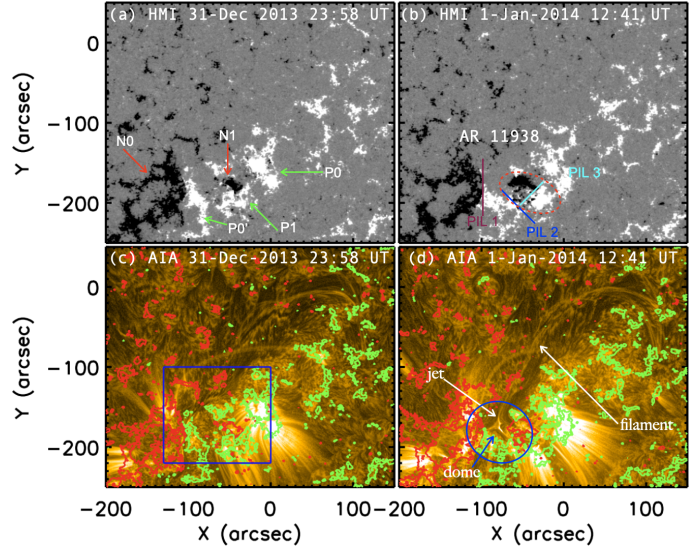


Fig. 9. Evolution of magnetic field (top row) and filament channel in AIA 171 \AA (bottom row) for event 2. The AR 11938 consists of a large positive polarity patch ($P0'$, $P0$, and $P1$) surrounded with negative polarities ($N0$, $N1$). The different PILs (1, 2, 3) are shown in panel b. The filament appears as dark areas (panel c-d) and the bright thin loops are possibly arcades or magnetic field lines of the filament structure. The jet flowing towards the filament channel near the PIL2 is shown with an arrow in panel d. The dome and null-point-like structure is enclosed by a blue circle. The green and red contours in the bottom row are the HMI magnetic field contours of ± 50 Gauss in strength, respectively. All images are aligned together at January 1, 2014, at 15:56 UT. The blue rectangular box is the FOV for Fig. 13.

Similarly to the previous event (Sects. 3.2 and 3.3), we can analyse the velocity of the jet and the oscillatory pattern using the same curved slit for both determinations, as shown in Fig. 11a. Concentrating here on the jet velocity, Fig. 11b shows the time–distance diagram for the AIA171 intensity along the slit in the first 120 min. The initial jet activity (before approximately 12:45 UT) is clearly seen in the form of bright features moving along the slit. These early jets all have a similar velocity; using a bright feature that starts at 12:42 UT, we obtain a speed of $\sim 120 \text{ km s}^{-1}$, as indicated with a dotted line on the left of the panel. Later, at 13:22 UT, we can identify an almost vertical brightening stretching between $100''$ and $150''$ and followed by a more gradual arch-like collection of brightenings all the way to the right end of the panel. The inclination of the almost vertical brightening corresponds to a propagation velocity of about 1000 km s^{-1} (dashed line in Fig. 11b). Continuing that dashed line towards the origin of the slit, one can see that it reaches the neighbourhood of what appears to be a counterpart of the semi-vertical brightening near the dome+null-point region. Still, it is not possible to find any causal connection between the two brightenings: we cannot identify in any of the EUV AIA channels anything propagating along the slit that could cause the filament to brighten in the $100''$ – $150''$ region of the slit as a result of the activity near the null-point region. Moving now to the arch-like brightenings, we can clearly identify velocities between 40 and 55 km s^{-1} in the initial part of the arches. Looking further in time (Fig. 11c), one sees that the arches are the initial part of oscillatory features in the filament (to help the identification, the location of panel b is indicated in panel c with a white rectangle). These are analysed in the following section.

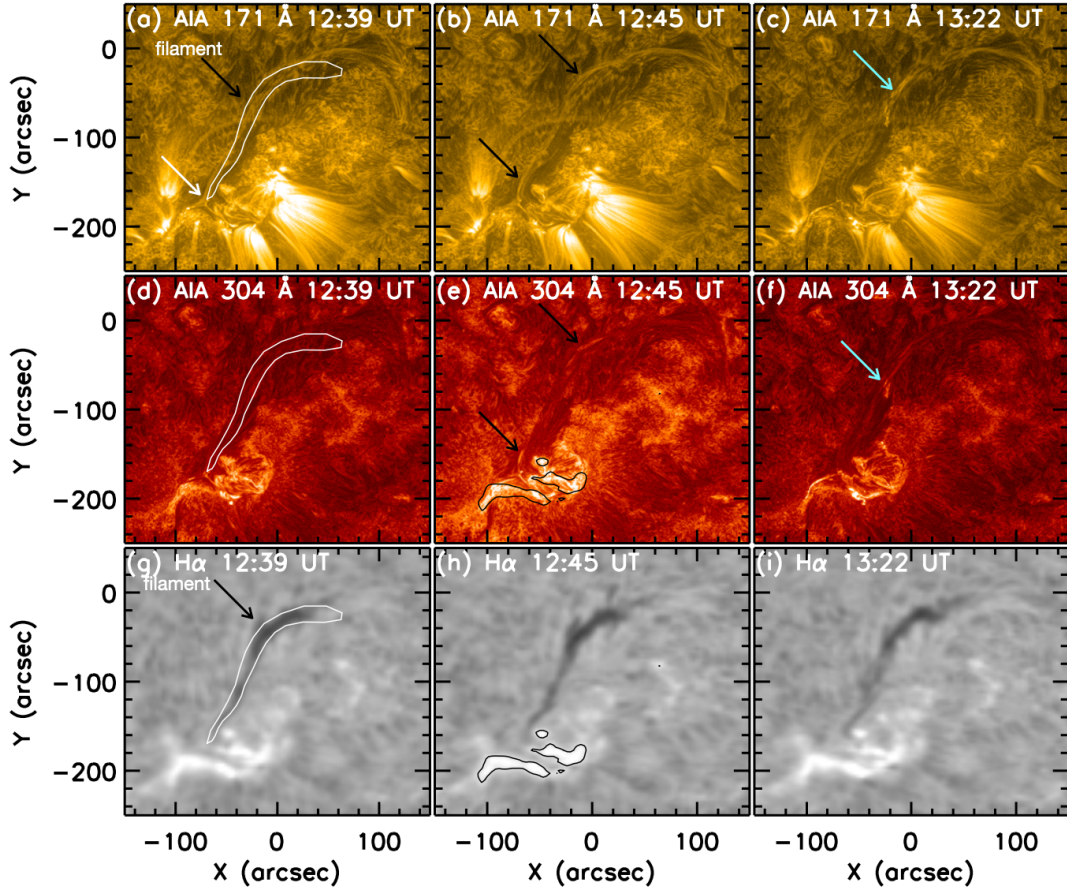


Fig. 10. Filament and jet evolution on January 1, 2014 (event 2), in AIA 171 Å (top row), AIA 304 Å (middle row), and H α (bottom row). The null-point-like structure is shown with a white arrow in panel a at the top of the dome-like structure. The jet propagation from this null-point towards the filament channel is shown with black arrows in panels b and e. The cyan arrows in panels c and f show the later brightening associated with the jet, which reinforces the oscillations. The filament is very well observed in H α as a dark long structure shown with black arrow in panel g indicating the sinistral handedness of the filament. The contours of the filament observed in H α are over-plotted in AIA 171 and 304 Å channels in panels a, b, and d. The black contours in panels e and h are for the brightening at the jet base observed in H α over-plotted in AIA 304 Å.

4.3. Filament oscillations

We focus now on the oscillatory patterns that start at $\sim 13:20$ UT following the almost vertically propagating brightening discussed immediately above and that last for more than 4 hours. In contrast to the February event, the oscillations here are more clearly discernible with all the threads oscillating approximately in phase. The oscillation can be distinguished until 18:00 UT. A fit to one of the oscillatory patterns gained through Eq. (1) can be seen through the white curve on the panel, with the parameters of the fit indicated on the top right. The period is 74 ± 1 min, which is in agreement with the results of the catalogue by Luna et al. (2018), and the damping time is 165 ± 23 min, which is almost in agreement with the catalogue value of 121 ± 15 min when considering the error bars. Using Eq. (2), we obtain a radius of curvature of the dipped field lines of $R = 170$ Mm. Also, Eq. (3) gives the minimum field value to support the cold plasma of the prominence against gravity. With the periods obtained, we can find the range of minimum values of the field intensity: $B_{\min} = 11\text{--}35$ Gauss. As mentioned in the previous event, by studying the oscillations with a slit, we can determine the amplitude, period, and damping time. However, the slit covers a restricted area of the filament. Using the technique introduced by Luna et al. (2022a) for this case, as we did for the February event

described in Sect. 3.3, we can see the main oscillation periods in the whole filament (see Fig. 12).

It can be seen that almost the entire filament oscillates and that the periods in the different regions range from 50 to 90 min, but predominantly near 80_{-8}^{+10} min. This value is in agreement with the value obtained with the slit analysis. Using this range of periods we obtain a range of radii of curvature 69–285 Mm and a minimum field intensity of 7–46 G.

4.4. Comparison of the observations to the theoretical model

As for the jets discussed in Sect. 3.4, the January 1 event shows some striking similarities to the Luna & Moreno-Insertis (2021) model. The basic underlying magnetic configuration of the model described in Sect. 3.4 is also present here, namely an arcade associated with a bipolar parasitic zone at one end of the FC surmounted by a null X-point. Three snapshots along the time evolution that are particularly relevant for the comparison are shown in Fig. 13 using AIA 171 Å maps. In panel a, taken from the map at $t = 12:03$ UT, an arcade is clearly seen at the southern end of the filament: going from the arcade upwards, the remote connectivity of the magnetic field and its orientation change abruptly at a point resembling an X-crossing: all of this

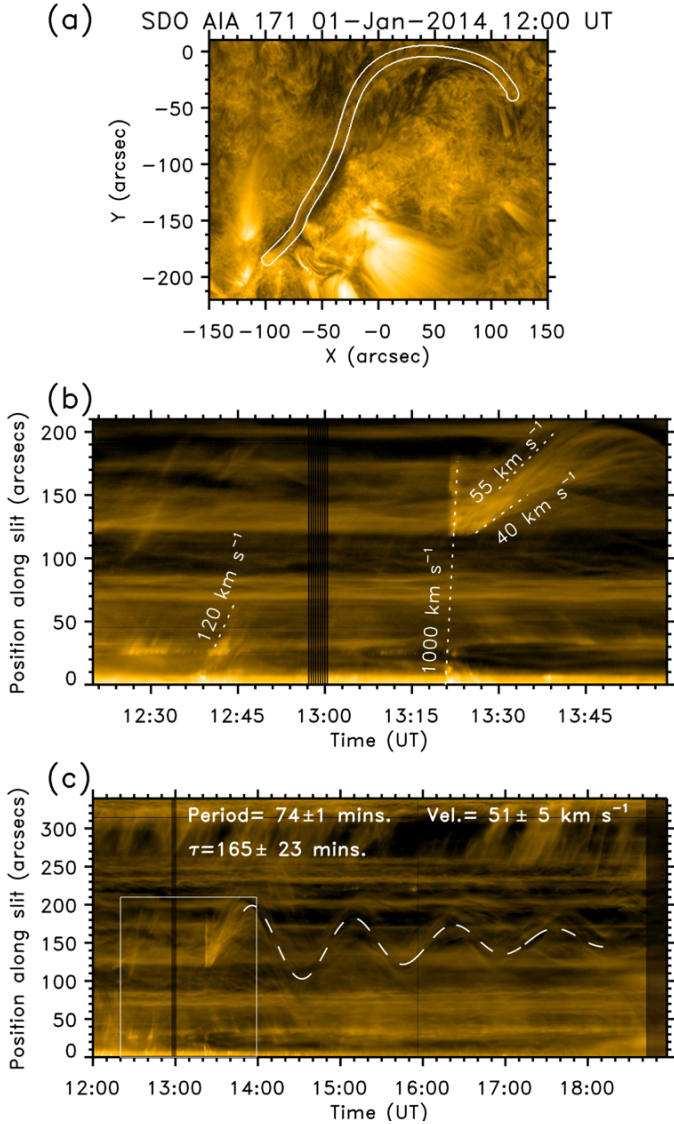


Fig. 11. Trace of the oscillations in the filament for the second event on January 1, 2014, observed with AIA 171 Å. Here we show the filament seen in absorption in AIA 171 Å. The artificial slit is shown as a white contour shown in panel a to construct the time–distance diagram shown in panels b and c.

indicates the probable presence of a null-point at the top of the arcade.

Photospheric shear at the feet of the arcade causes the null-point to become a BCS where reconnection takes place. In fact, at the later time shown in panel b ($t = 12:31$ UT), at the location of the null-point, one sees a structure with a clear H-shape, which probably corresponds to the BCS. The flows emanating from it are directed mainly toward the filament, but also in the opposite direction. From the model, we expect this to correspond to the quiescent phase of the jet, with continuous plasma flows emanating from the reconnection site. The resemblance to the numerical model is remarkable, as can be gathered by comparing the observed structure with that in the inset, adapted from the Luna & Moreno-Insertis (2021) paper, which contains a colour map of the module of the electric current with velocity arrows superimposed. In the numerical model, the reconnection in the BCS ceases later on, but by then the arcade has become elongated in the vertical direction and an intense vertical current

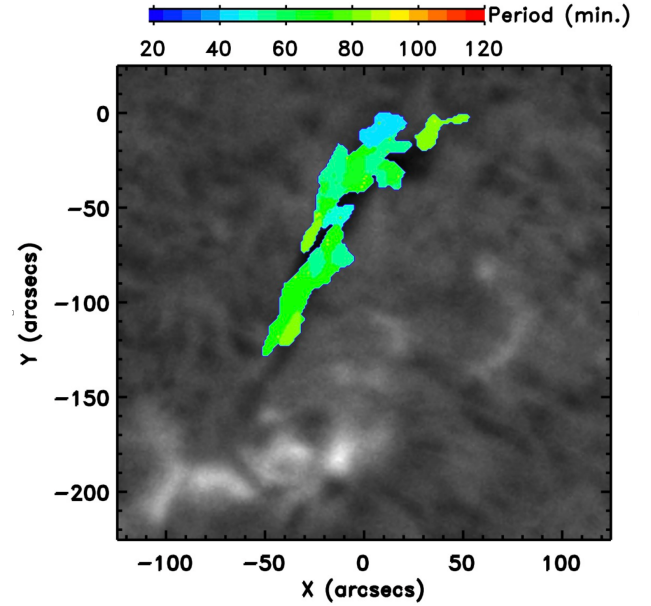


Fig. 12. Time periods of the filament oscillations over a GONG $H\alpha$ image on January 1, 2014, using the technique developed by Luna et al. (2022a). The colour code shows the periods in minutes.

sheet appears at its centre; there follows reconnection across that current sheet, and a violent jet is ejected along the filament channel.

Panel c, taken from the AIA171 map at $t = 13 : 21$ UT, corresponds to this phase, with a brightening along the field lines indicated by the cyan arrow. That brightening could be associated with the eruptive phase, in which a plasmoid or mini filament is ejected. The eruption as described in the model is not identifiable. However, these brightenings indicate that an energetic process has taken place. As an additional indication of the violence of the process, the oscillation of the filament starts immediately after this brightening, as we describe in Sect. 4.3.

5. Conclusion

This observational study was inspired by the scenario recently proposed by Luna & Moreno-Insertis (2021) for triggering LAOs in filaments. The authors propose that the LAOs may be initiated by jets in a reconnection process in the magnetic structure of the filament. We identified two case studies that show similarities to the model. In both cases, we analysed observational data to understand how the oscillation starts and how the filament oscillates after this perturbation. In the first case, occurring on February 5, 2015, the jet perturbs a large portion of the $H\alpha$ filament that oscillates mainly with a period of 74 min. The period detected in 171 Å is not as clearly defined, ranging from 70 to 110 min, leading us to believe that the filament is made by different structures at different altitudes. In the second case, on January 1, 2014, a large portion of the $H\alpha$ filament is perturbed as well, and the oscillations have a range of periods of 50–90 min. In both cases, periods reaching 120 min are detected.

These values for the period are consistent with those of typical LAOs and with the results from the catalogue of Luna et al. (2018). We applied prominence seismology using the pendulum model by Luna et al. (2012, 2022b), which allowed us to compute the curvature of the dips in the flux rope containing the filament, and the magnetic field strength. The latter has been estimated to be of the order of 30 Gauss in

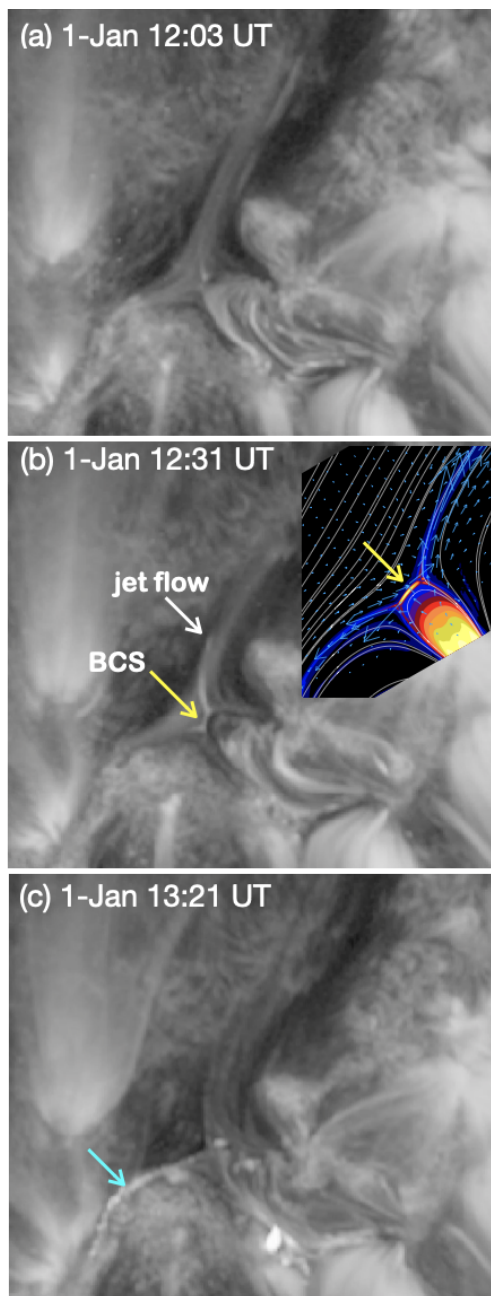


Fig. 13. Zoom onto the jet base region in 171 Å maps as indicated with the blue rectangular box in Fig. 9c. The three panels show three stages of the temporal evolution of the jet. Panel a shows an X-point structure can be identified in the central part. This structure evolves and acquires a BCS H-type shape marked by the white arrow. Important flows are seen emanating from the H structure. The inset in panel b shows the electric currents distribution from the Luna & Moreno-Insertis (2021) model (adapted from their Fig. 4b). The white curves are the magnetic field lines and the blue vectors are the velocities of the plasma. Finally, in panel c, this structure disappears and a brightening is seen around it. The cyan arrow in panel c shows the brightening along the field lines associated with the eruptive phase. Associated animation is available [online](#).

both filaments. These values are in agreement with direct measurements from observations (Leroy et al. 1984; Levens et al. 2016, 2017). Both cases described in this work are intermediate filaments with one end connected to ARs and the magnetic field can be rather large (López Ariste & Aulanier 2007;

Díaz Baso et al. 2019). Luna et al. (2017), and more recently Kucera et al. (2022), showed that the seismological predictions of the pendulum model work well and give similar results for the field geometry and field strength to other techniques.

Both events show similarities to the Luna & Moreno-Insertis (2021) model. Both show a quadrupolar structure with a parasitic bipole at one end of the filament channel. On top of this parasitic polarity, there is a classical X-shaped structure in the AIA brightenings that strongly resembles a null-point configuration. In both cases, the parasitic polarity is produced by magnetic flux emergence. There is also a strong shear along the polarity inversion line, which may be responsible for disturbing the null-point and producing the magnetic reconnection that leads to the jet. A structure with the appearance of a BCS can be identified, which surprisingly resembles the structures obtained in the Luna & Moreno-Insertis (2021) numerical simulations.

In the first observed event (February 5, 2015), the formation of the BCS is followed by the eruption of a mini filament. This indicates that both the quiescent and eruptive phases of the jet occur almost at the same time, in contrast to the model. This may be due to the fact that the magnetic shear injection in the parasitic region is higher than in the model. In the model, we did not explore the possibility of increasing the injection rate, which will be left for a future study. When the jet is launched, part of it almost directly impacts the dense material in the filament, but part of it runs along the overarching field lines. One interpretation is that the filament is sitting at the bottom of the main dips of a flux rope, but the field lines above the filament are arched, and perhaps also moderately twisted around the filament as in Aulanier & Schmieder (2002).

In the second event (January 1, 2014), the BCS-like structure is observed for a long time, which, as in the previous case, is in agreement with the model. We identify this first phase as quiescent; the emanating jet does not seem to impact the filament because it does not produce oscillations. These flows probably travel along field lines of the filament channel without threads. As seen in the numerical modelling, the initial height of the null point relative to the filament determines how the different phases of the jet impact the filament. After some time, a sudden brightening around the parasitic zone is observed, which could be identified with the eruptive phase of the jet. After this brightening, the filament starts to oscillate with a large amplitude motion. However, we cannot identify any plasma flow from the jet area to the filament. Perhaps, the plasma moves along field lines that are partially hidden by the filament itself or by the foreground emission of coronal structures. The triggering of the oscillations in this second event could be caused by activity unrelated to the null-point. However, we did not observe plasma flows reaching the filament from other regions. An alternative explanation could be that some disturbance (e.g., reconnection) produces changes in the magnetic structure of the filament that disturb its cold plasma.

Still, the direct impact of jets remains the most probable cause of the filament oscillations in the first event. Interestingly, a preprint published after submission of the present manuscript reports another event where filament oscillations are caused by jets, also showing clear bilateral flows (Tan et al. 2023).

Nevertheless, we conclude that the events presented here bear a clear resemblance to those described in the model by Luna & Moreno-Insertis (2021). A comprehensive study of the triggering processes of LAOs in filaments is needed to better understand these processes. A numerical study is also needed

to investigate how the jet synthesis is affected by different parameters such as boundary driving. It is also necessary to extend the study to three dimensions.

Acknowledgements. We acknowledge the anonymous referee for the valuable/constructive comments and suggestions. This research has been supported by the European Research Council through the Synergy Grant number 810218 (“The Whole Sun”, ERC-2018-SyG) and by the Research Council of Norway through its Centres of Excellence scheme, project number 262622. M.L. acknowledges support through the Ramón y Cajal fellowship RYC2018-026129-I from the Spanish Ministry of Science and Innovation, the Spanish National Research Agency (Agencia Estatal de Investigación), the European Social Fund through Operational Program FSE 2014 of Employment, Education and Training and the Universitat de les Illes Balears. This publication is part of the R+D+I project PID2020-112791GB-I00, financed by MCIN/AEI/10.13039/501100011033. Funding by the Spanish Ministry of Science, Innovation and Universities through project PG2018-095832-B-I00 is also gratefully acknowledged. This work benefited from discussions at the International Space Science Institute (ISSI) in Bern, through ISSI International team project 535 “Unraveling Surges: a joint perspective from numerical models, observations, and machine learning.”

References

- Adrover-González, A., & Terradas, J. 2020, *A&A*, **633**, A113
- Asai, A., Ishii, T. T., Isobe, H., et al. 2012, *ApJ*, **745**, L18
- Aulanier, G., & Schmieder, B. 2002, *A&A*, **386**, 1106
- Chen, H. D., Jiang, Y. C., & Ma, S. L. 2008, *A&A*, **478**, 907
- Devi, P., Chandra, R., Joshi, R., et al. 2022, *Adv. Space Res.*, **70**, 1592
- Díaz Baso, C. J., Martínez González, M. J., Asensio Ramos, A., & de la Cruz Rodríguez, J. 2019, *A&A*, **623**, A178
- Eto, S., Isobe, H., Narukage, N., et al. 2002, *PASJ*, **54**, 481
- Freeland, S. L., & Handy, B. N. 1998, *Sol. Phys.*, **182**, 497
- Gibson, S. E. 2018, *Liv. Rev. Sol. Phys.*, **15**, 7
- Hyder, C. L. 1966, *ZAp*, **63**, 78
- Isobe, H., Tripathi, D., & Archontis, V. 2007, *ApJ*, **657**, L53
- Jing, J., Lee, J., Spirock, T. J., et al. 2003, *ApJ*, **584**, L103
- Joshi, R. 2022, Ph.D. Thesis, Norway [arXiv:2206.02478]
- Joshi, R., Chandra, R., Schmieder, B., et al. 2020a, *A&A*, **639**, A22
- Joshi, R., Schmieder, B., Aulanier, G., Bommier, V., & Chandra, R. 2020b, *A&A*, **642**, A169
- Joshi, R., Schmieder, B., Heinzel, P., et al. 2021a, *A&A*, **654**, A31
- Joshi, R., Schmieder, B., Tei, A., et al. 2021b, *A&A*, **645**, A80
- Kucera, T. A., Luna, M., Török, T., et al. 2022, *ApJ*, **940**, 34
- Labrosse, N., Heinzel, P., Vial, J. C., et al. 2010, *Space Sci. Rev.*, **151**, 243
- Lemen, J. R., Title, A. M., Akin, D. J., et al. 2012, *Sol. Phys.*, **275**, 17
- Leroy, J. L., Bommier, V., & Sahal-Brechot, S. 1984, *A&A*, **131**, 33
- Levens, P. J., Schmieder, B., López Ariste, A., et al. 2016, *ApJ*, **826**, 164
- Levens, P. J., Labrosse, N., Schmieder, B., López Ariste, A., & Fletcher, L. 2017, *A&A*, **607**, A16
- Li, T., & Zhang, J. 2012, *ApJ*, **760**, L10
- Liakh, V., Luna, M., & Khomenko, E. 2020, *A&A*, **637**, A75
- Liakh, V., Luna, M., & Khomenko, E. 2021, *A&A*, **654**, A145
- Liu, W., Ofman, L., Nitta, N. V., et al. 2012, *ApJ*, **753**, 52
- López Ariste, A., & Aulanier, G. 2007, *ASP Conf. Ser.*, **368**, 291
- Luna, M., & Karpen, J. 2012, *ApJ*, **750**, L1
- Luna, M., & Moreno-Insertis, F. 2021, *ApJ*, **912**, 75
- Luna, M., Díaz, A. J., & Karpen, J. 2012, *ApJ*, **757**, 98
- Luna, M., Knizhnik, K., Muglach, K., et al. 2014, *ApJ*, **785**, 79
- Luna, M., Terradas, J., Khomenko, E., Collados, M., & de Vicente, A. 2016, *ApJ*, **817**, 157
- Luna, M., Su, Y., Schmieder, B., Chandra, R., & Kucera, T. A. 2017, *ApJ*, **850**, 143
- Luna, M., Karpen, J., Ballester, J. L., et al. 2018, *ApJS*, **236**, 35
- Luna, M., Mérou Mestre, J. R., & Auchère, F. 2022a, *A&A*, **666**, A195
- Luna, M., Terradas, J., Karpen, J., & Ballester, J. L. 2022b, *A&A*, **660**, A54
- Mackay, D. H., Karpen, J. T., Ballester, J. L., Schmieder, B., & Aulanier, G. 2010, *Space Sci. Rev.*, **151**, 333
- Morgan, H., & Druckmüller, M. 2014, *Sol. Phys.*, **289**, 2945
- Ofman, L., Knizhnik, K., Kucera, T., & Schmieder, B. 2015, *ApJ*, **813**, 124
- Okamoto, T. J., Nakai, H., Keiyama, A., et al. 2004, *ApJ*, **608**, 1124
- Parenti, S. 2014, *Liv. Rev. Sol. Phys.*, **11**, 1
- Parenti, S., Schmieder, B., Heinzel, P., & Golub, L. 2012, *ApJ*, **754**, 66
- Pesnell, W. D., Thompson, B. J., & Chamberlin, P. C. 2012, *Sol. Phys.*, **275**, 3
- Raes, J. O., Van Doorselaere, T., Baes, M., & Wright, A. N. 2017, *A&A*, **602**, A75
- Ramsey, H. E., & Smith, S. F. 1966, *AJ*, **71**, 197
- Roberts, B. 2019, *MHD Waves in the Solar Atmosphere* (Cambridge: Cambridge University Press)
- Sainz Dalda, A., & Bellot Rubio, L. R. 2008, *A&A*, **481**, L21
- Schmieder, B. 2022, *Front. Astron. Space Sci.*, **9**, 820183
- Schmieder, B., Kucera, T. A., Knizhnik, K., et al. 2013, *ApJ*, **777**, 108
- Schmieder, B., Joshi, R., & Chandra, R. 2022, *Adv. Space Res.*, **70**, 1580
- Schou, J., Scherrer, P. H., Bush, R. I., et al. 2012, *Sol. Phys.*, **275**, 229
- Shen, Y., Liu, Y. D., Chen, P. F., & Ichimoto, K. 2014, *ApJ*, **795**, 130
- Tan, S., Shen, Y., Zhou, X., et al. 2023, *MNRAS*, **520**, 3080
- Vršnak, B. 1993, *Hvar Obs. Bull.*, **17**, 23
- Vršnak, B., Veronig, A. M., Thalmann, J. K., & Žic, T. 2007, *A&A*, **471**, 295
- Zhang, Q. M., Chen, P. F., Guo, Y., Fang, C., & Ding, M. D. 2012, *ApJ*, **746**, 19
- Zhang, Q. M., Li, D., & Ning, Z. J. 2017, *ApJ*, **851**, 47
- Zhang, L. Y., Fang, C., & Chen, P. F. 2019, *ApJ*, **884**, 74
- Zhou, Y.-H., Xia, C., Keppens, R., Fang, C., & Chen, P. F. 2018, *ApJ*, **856**, 179